applied sciences

MDPI

Article

Fracture Propagation Characteristics and Borehole Spacing Optimization of Bidirectional Shaped-Charge Blasting in the Hard Roof of a Deep-Buried Coal Seam

Pengfei Shan [1,2], Yansheng Ma [1,*], Xiaomin Wang [1], Xiaochen Wu [1,3], Kun Chen [3], Wenlin Wang [3], Wenhua Yang [1,2] and Huicong Xu [1,2,*]

[1] College of Energy and Mining Engineering, Xi'an University of Science and Technology, Xi'an 710054, China
[2] Key Laboratory of Western Mine Exploration and Hazard Prevention, Ministry of Education, Xi'an University of Science and Technology, Xi'an 710054, China
[3] Shaanxi Huabin Yadian Coal Industry Co., Ltd., Binzhou 713500, China
* Correspondence: kuangye1232026@163.com (Y.M.); xhcxust@163.com (H.X.)

Abstract

To address severe mining-roadway deformation induced by roof stress concentration resulting from delayed fracture and caving of deep-buried thick and hard roofs, the ZC1103 working face of Yadian Coal Mine was selected as the engineering background. A fracture criterion based on the crack-tip stress intensity factor and rock fracture toughness was introduced to analyze fracture propagation and arrest along the shaped-charge direction. Bidirectional shaped-charge blasting models with different blasthole spacings were established using ANSYS and LS-DYNA, and multi-hole synergistic fracturing was evaluated from fracture coalescence, inter-hole pressure response, and overlap of damaged zones, followed by field validation. Results show that the bidirectional shaped-charge structure significantly alters the spatial distribution of blast-induced pressure around the blasthole. At 100 and 200 mm from the blasthole center, peak pressures in the shaped-charge direction increased by 48.9% and 35.1%, respectively, relative to conventional blasting, whereas those in the non-shaped-charge direction decreased by 28.0% and 34.9%, respectively. Field tests showed that, at a blasthole spacing of 1.0 m, distinct fracture traces were observed on the borehole wall 0.5 m from the adjacent blasthole, while the borehole walls remained largely intact. Compared with the non-pressure-relief zone, the cumulative deformation of the solid-coal rib, gob-side rib, and roof in the roof-cutting pressure-relief zone was lower by 41.7%, 51.8%, and 38.9%, respectively. These results provide a reference for designing bidirectional shaped-charge blasting spacing under similar deep-buried thick-and-hard-roof conditions based on fracture propagation and inter-hole coalescence criteria.

Keywords: thick and hard roof; bidirectional shaped-charge blasting; surrounding rock deformation; roof cutting and pressure relief; directional fracturing

Check for updates

Academic Editor: Nikolaos Koukouzas

Received: 14 September 2026
Revised: 19 October 2026
Accepted: 22 October 2026
Published: 25 October 2026

Copyright: © 2026 by the authors. Licensee MDPI, Basel, Switzerland. This article is an open access article distributed under the terms and conditions of the Creative Commons Attribution (CC BY) license.

1. Introduction

As coal mining extends to greater depths, the combined effects of high in situ stress and intense mining-induced disturbance pose increased challenges to ground control during longwall extraction [1–3]. Thick and hard roofs above the working face are generally strong and intact and therefore tend to cave slowly after extraction, leaving a suspended roof on the gob side. Such overhanging structures intensify stress concentration and deformation in the surrounding rock, while stress redistribution can further promote progressive damage,

crack propagation, and eventual instability of the rock mass [4–6]. Active weakening of the roof and deliberate control of its fracture position have therefore become important strategies for ground control in high-stress roadways.

Considerable research has been devoted to mitigating severe ground pressure and controlling roadway deformation beneath hard roofs, with hydraulic fracturing, dense drilling, and blasting-induced weakening being the principal active pressure-relief approaches [7,8]. Borehole-based destressing is also an effective active pressure-relief approach for deep roadways. Dai et al. [9] developed an energy-based method for evaluating the active energy-releasing capacity of destressing boreholes and examined its applicability to roadway rockburst mitigation. Hydraulic fracturing weakens hard roofs by driving crack initiation and propagation through high-pressure fluid injection. Li et al. [10] used fracture mechanics to clarify the effects of in situ stress, pre-cut slot parameters, and fluid pressure on the crack-initiation pressure and propagation direction in hard roofs. Zhuang et al. [11] achieved regional weakening of thick and hard roofs through multistage hydraulic fracturing in horizontal long boreholes and demonstrated its effectiveness in controlling coal bursts. Dense drilling, by contrast, reduces the effective load-bearing cross-section of the roof and promotes the coalescence of damage zones between adjacent boreholes under mining-induced loading. Liu et al. [12] showed that borehole diameter, spacing, drilling height, and inclination are key parameters governing fracture development and the roof-cutting effectiveness of densely drilled holes. Ma et al. [13] found that increasing borehole diameter or reducing borehole spacing promotes the interaction and coalescence of plastic zones around adjacent boreholes, facilitating the formation of a continuous weakened zone under mining-induced loading. However, hydraulic-fracture initiation and propagation are strongly influenced by the in situ stress field and roof stratigraphy, making fracture-pressure control and directional propagation increasingly demanding under deep, high-stress conditions. Dense drilling, meanwhile, relies on a relatively high borehole density and can therefore require substantial drilling effort for deep boreholes and long-distance treatment of thick and hard roofs. Blasting-induced weakening offers a more rapid means of generating an extensive fracture-damage zone through the combined action of blast stress waves and detonation gases. Experimental and numerical investigations by Zhu et al. [14] showed that shaped-charge blasting promotes the formation of pronounced directional main fractures, improves the directional utilization of explosive energy, and reduces disturbance in non-target regions. Liu et al. [15] found that, under the same blasting conditions, the energy concentration and fracture extension along the shaped-charge direction were markedly greater than those under conventional blasting. The author of [16] established a mechanical model of the roof-breaking structure in gob-side entry retaining and showed that roof cutting can weaken the mechanical connection between the gob-side roof and the retained-roadway roof, thereby reducing the influence of overlying key-block movement on roadway stability. Yu et al. [17] proposed a composite directional blasting technique for hard-roof slitting, in which a shaped-charge jet first creates an initial directional channel and subsequent high-pressure gas drives further fracture propagation. Ma et al. [18] further investigated shaped-charge-jet penetration into a hard roof using an ALE-based LS-DYNA model and characterized the resulting penetration-channel geometry and surrounding rock damage. Collectively, these studies demonstrate that shaped-charge blasting combines strong fracturing capability with enhanced directional control, providing an effective approach for forming continuous directional fractures in thick and hard roofs.

Experimental studies have confirmed the directional fracturing characteristics of shaped-charge blasting. However, because blasting is highly transient and the internal response of the rock is difficult to observe directly, experimental methods alone provide limited access to the continuous evolution of stress-wave propagation and internal fracture

development. Liu et al. [19] combined drilling-and-blasting model tests, numerical simulations, and field applications to investigate directional damage-reduction shaped-charge blasting, showing that the charge structure promotes directional fracture development while reducing blasting disturbance in the protected direction. Numerical simulation, therefore, provides an important means of resolving the transient processes governing shaped-charge fracturing, including blast stress-wave propagation, detonation-gas-driven fracture growth, and dynamic crack evolution. Ding et al. [20] investigated stress-wave superposition and crack initiation between two adjacent boreholes through model tests and numerical simulations and showed that crack initiation in the inter-borehole stress-wave superposition zone depends strongly on explosive parameters, rock properties, and borehole spacing. Meng et al. [21] investigated the effects of in situ stress on rock damage and fracture propagation during shaped-charge jet blasting and showed that both the extent and directional characteristics of blasting-induced fractures are significantly affected by the magnitude and anisotropy of the in situ stress field. Meng et al. [22] used LS-DYNA to investigate directional fracturing between adjacent shaped-charge blastholes and analyzed the evolution of the shaped-charge jet, equivalent stress, and main and secondary fractures during the blasting process. Wu et al. [23] investigated the dynamic evolution of blasting-induced cracks in elliptical bipolar linear shaped-charge blasting using LS-DYNA simulations and laboratory tests, demonstrating pronounced directional crack formation along the shaped-charge direction. These studies have substantially advanced the understanding of load transmission, fracture initiation, and fracture propagation during shaped-charge blasting. Previous studies have also investigated stress-wave interaction, fracture initiation, and fracture coalescence between adjacent blastholes. However, the integration of these multi-blasthole interaction mechanisms into a spacing-selection framework for continuous bidirectional shaped-charge roof cutting under deep-buried thick and hard roof conditions remains relatively limited. In particular, a systematic procedure that links single-blasthole directional fracture capacity, fracture propagation and arrest, and the interaction of fractures between adjacent blastholes to engineering blasthole-spacing selection has not been sufficiently established for such roof conditions.

To address this gap, the ZC1103 working face of Yadian Coal Mine was selected as the engineering background to investigate fracture propagation and blasthole-spacing effects under bidirectional shaped-charge blasting. A theoretical framework for blasthole-spacing control was established by combining the directional fracture-initiation mechanism of shaped-charge blasting, detonation-gas-driven fracture propagation, a fracture-mechanics criterion for crack-tip growth, blast-load attenuation, and the fracture-interaction requirement between adjacent blastholes. Numerical models with different blasthole spacings were then developed to evaluate fracture interaction, inter-blasthole coalescence, and damage evolution at different spacings, followed by field observations. The study therefore develops a blasthole-spacing determination framework that integrates theoretical constraints on fracture propagation, numerical evaluation of multi-blasthole fracture interaction, and field observations, providing a basis for selecting bidirectional shaped-charge roof-cutting parameters under similar thick and hard roof conditions.

2. Engineering Background

2.1. Mining Conditions

Yadian Coal Mine, located in the Huanglong mining area of Binzhou City, Shaanxi Province, is situated in the Loess Plateau, where the surface terrain is characterized by ridge, tableland, and gully landforms with intense topographic dissection. The ZC1103 longwall face in the No. 1 mining district was selected as the engineering case. The face has a strike length of 3060 m and a cover depth of 624–781 m. The coal seam occurs relatively

consistently, with an average minable thickness of 2.6 m and a dip angle of 0–5°. Fully mechanized longwall mining with single-pass, full-seam-height extraction is employed, with full caving adopted for roof management. The false roof of the No. 1 coal seam is mudstone that is prone to weathering and fragmentation. The direct roof is grey-green siltstone with well-developed fractures filled with gypsum. The main roof comprises grayish-white, medium-grained sandstone with argillaceous–calcareous cementation and locally contains fine quartz pebbles. The layout of the ZC1103 longwall face is shown in Figure 1, and its geological columnar section is presented in Figure 2.

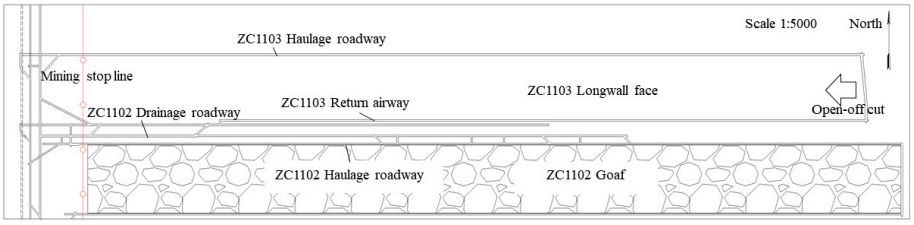


Figure 1. Layout of the ZC1103 longwall face.

No.	Bedded	Thickness	Burial depth	Lithology
1		144.50m	144.50m	Loess
2		150.90m	295.40m	Siltstone
3		342.60m	638.00m	Coarse-grained sandstone
4		25.50m	663.50m	Conglomerate
5		2.90m	666.40m	Mudstone
6		1.00m	667.40m	Fine-grained sandstone
7		9.10m	676.50m	Mudstone
8		4.20m	680.70m	Siltstone
9		1.00 m	681.70m	Mudstone
10		4.40m	686.10m	Siltstone
11		11.65m	692.75m	Fine-grained sandstone
12		1.35m	694.10m	Siltstone
13		11.50m	705.60m	Coarse-grained sandstone
14		10.00m	715.60m	Siltstone
15		0.60m	721.60m	Mudstone
16		2.95m	721.80m	1 coal seam
17		1.50m	723.30m	Mudstone
18		13.50m	736.80m	Fine-grained sandstone
19		1.50m	738.30m	Medium-grained sandstone
20		2.00m	740.30m	Siltstone
21		10.80m	748.50m	Mudstone
22		8.20m	759.30m	Sandy mudstone
23		1.90m	761.20m	Mudstone
24		11.30m	772.50m	4 coal seam
25		1.10m	773.60m	Sandy mudstone
26		2.40m	776.00m	Mudstone
27		11.68m	787.68m	Siltstone

Figure 2. Composite geological columnar section of the ZC1103 longwall face.

For the ZC1103 working face, the relatively large burial depth and the development of sandstone strata in the overlying roof create unfavorable conditions for roof control. In particular, the main roof is thick, competent, and highly intact. Under the combined effects of overburden loading and the thick, hard roof, the main roof is prone to delayed breakage after extraction, allowing a large suspended roof to develop. The resulting load transfer toward the roadway and the solid-coal side intensifies local stress concentration and leads to pronounced ground-pressure behavior. High compressive stress also suppresses the initiation and propagation of tensile fractures to some extent, making it more difficult to form a continuous fracture plane along the prescribed direction. Therefore, artificial pre-splitting is required to weaken the integrity of the thick and hard roof and control its fracture path. Bidirectional shaped-charge blasting concentrates explosive energy along the designed roof-cutting direction, thereby enhancing crack initiation and propagation in the target direction. This promotes the formation of a continuous pre-fractured weak plane within the thick and hard main roof and facilitates active roof cutting and pressure relief.

2.2. Deformation and Failure Characteristics of the Surrounding Rock in the Return Airway

Following extraction of the ZC1103 longwall face, the gob-side main roof did not cave promptly and gradually formed a suspended roof structure extending over the gob. As the face advanced, the suspended-roof load was transferred through the main roof to the return airway and the solid-coal side, subjecting the roadway to the combined effects of mining-induced abutment pressure and the additional load imposed by the suspended roof. Field observations revealed roof subsidence, floor heave, and deformation of both ribs, as illustrated in Figure 3.



（a） Roof subsidence （b） Floor heave （c） Rib deformation

Figure 3. Surrounding-rock deformation characteristics of the ZC1103 return airway.

The ZC1103 return-air roadway exhibits localized roof subsidence, floor heave, and inward convergence of the two ribs after being disturbed by longwall extraction. Roof deformation is particularly pronounced. Because the false roof is extremely weak and unstable, separation readily develops between the false roof and the overlying immediate roof, resulting in large roof displacement accompanied by localized falls. The roadway ribs show asymmetric convergence and composite failure. Under the combined influence of high in situ stress and tectonic stress, the two ribs undergo distinctly uneven deformation toward the roadway opening. The floor is mainly composed of mudstone and sandy mudstone, both of which are prone to softening and swelling when exposed to water. Under high-stress conditions, the floor therefore exhibits persistent and severe heave. The deformation is typically characterized by overall uplift along the roadway centerline, together with dislocation and cracking of the floor strata, while pronounced grooves develop near the two floor corners because of compression against the roadway ribs.

Bidirectional shaped-charge blasting can generate fractures that preferentially propagate along a prescribed direction within the target stratum. When blasting holes are continuously arranged along the gob side of the return-air roadway, the directional fractures generated by adjacent boreholes must effectively coalesce within the inter-borehole region to form a continuous roof-cutting plane. If the borehole spacing is too large, adjacent fractures may fail to connect. Conversely, excessively small spacing can lead to excessive overlap of near-borehole damage zones, increased damage in the non-shaped-charge direction, and unnecessary increases in drilling and explosive-loading requirements. Accordingly, this study investigates inter-borehole fracture coalescence, damage-zone interaction, and stress-transfer characteristics under different borehole spacings for the medium-grained sandstone main roof of the ZC1103 working face, with the aim of determining a rational engineering spacing.

3. Mechanisms of Directional Fracture Propagation and Inter-Hole Coalescence in Bidirectional Shaped-Charge Blasting

3.1. Dynamic Loading and Initial Directional-Crack Formation in Bidirectional Shaped-Charge Blasting

The bidirectional shaped-charge structure redistributes the detonation products and blast loading, directing a greater proportion of the explosive energy toward the prescribed roof-cutting direction. Following initiation, the detonation waves near the shaped-charge

surfaces converge and superimpose, resulting in a higher equivalent peak pressure on the borehole wall along the shaped-charge direction than in the non-shaped-charge direction. This directional loading generates localized high-stress zones on both sides of the borehole. At this stage, the dominant response is localized crushing of the borehole wall accompanied by the initiation of directional fractures, rather than the immediate formation of a fully coalesced inter-borehole fracture. A schematic illustration of the directional energy release during bidirectional shaped-charge blasting is shown in Figure 4.

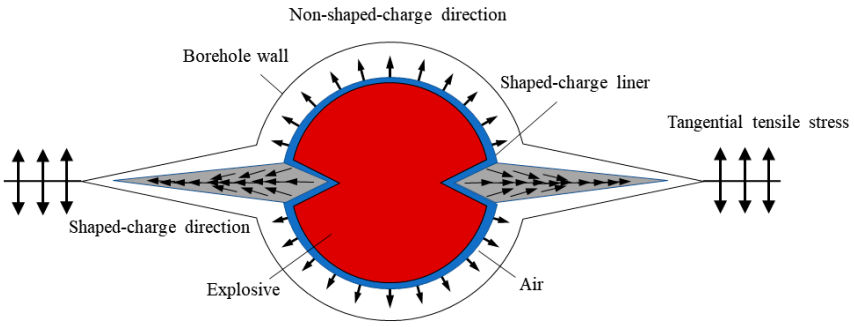


Figure 4. Schematic of directional energy release in bidirectional Shaped-Charge Blasting.

Based on blast dynamics theory, the initial detonation pressure generated by a cylindrical explosive charge in rock can be expressed as [24–26]:

$$P_0 = \frac{\rho_0 D^2}{1+\omega} \tag{1}$$

where P_0 is the initial detonation pressure, MPa; ρ_0 is the explosive density, kg/m^3; D is the detonation velocity of the explosive, m/s; and ω is the adiabatic expansion exponent of the detonation products, typically taken as 3.

According to explosion mechanics, when the incident angle of the detonation wave at the shaped-charge surface satisfies the condition for irregular oblique interaction, a Mach reflection wave forms along the shaped-charge direction. The post-reflection pressure can be approximately expressed as:

$$P_1 = \frac{2P_0}{1-\cos\varphi} \tag{2}$$

$$\varphi = \frac{\pi}{2} - \alpha \tag{3}$$

where P_1 is the post-wave pressure generated by Mach-wave superposition at the shaped-charge surface, MPa; α is the half-angle of the shaped-charge structure; and φ is the incident angle of the detonation wave during symmetric collision at the shaped-charge surface, with $\varphi = 60^\circ$. The resulting pressure acting on the borehole wall can then be expressed as [27]:

$$P_2 = \frac{1}{2} P_1 M^{-2\omega} l_c n \tag{4}$$

where P_2 is the maximum pressure acting on the borehole wall under decoupled charging, MPa; M is the charge decoupling coefficient; l_c is the axial charge coefficient, taken as 1; and n is the amplification coefficient for the expansion pressure of the detonation products, taken as 5. For the present blasting configuration, the radial charge-decoupling coefficient was M = 1.806. Using the adopted explosive and loading parameters, Equations (1)–(4) give P_0 = 9.69 GPa, P_1 = 38.76 GPa, and P_2 = 2.80 GPa. The initial directional-crack formation process under dynamic loading is schematically illustrated in Figure 5.

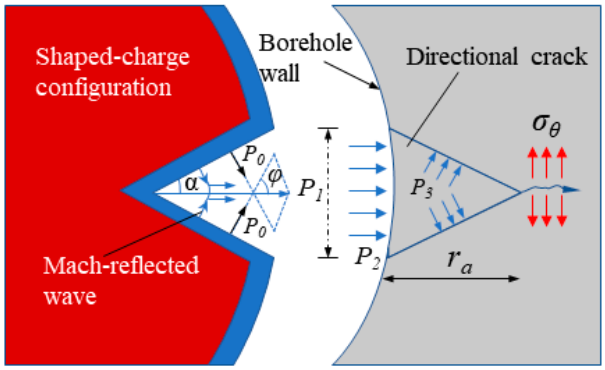


Figure 5. Schematic of initial directional-crack formation under dynamic loading.

When the circumferential tensile stress induced by the attenuated blast stress wave reaches the tensile failure threshold of the rock, initial directional fractures are generated around the blasthole wall:

$$r_a = \left(\frac{\eta P_2}{\sigma_t}\right)^{\frac{1}{\beta}} r_b \tag{5}$$

where r_a is the length of the initial directional fracture measured outward from the borehole wall during the dynamic blasting stage, m; r_b m is the borehole radius; $\eta = \mu/(1-\mu)$ is the lateral-stress correction coefficient, with $\mu = 0.234$; $\beta = 1.6945$ is the stress-wave attenuation exponent; and $\sigma_t = 12.5$ MPa is the tensile-strength parameter of the rock under blast loading. Combining Equations (1)–(5) gives $r_a = 0.393$ m. The corresponding expression can be written as:

$$r_a = \left\{\frac{\mu\rho_0 D^2 M^{-2\omega} l_c n}{(1-\mu)(1+\omega)\left[1-\cos\left(\frac{\pi-\alpha}{2}\right)\right]\sigma_t}\right\}^{\frac{1}{\beta}} r_b \tag{6}$$

3.2. Criterion for Crack-Tip Propagation in Shaped-Charge Blasting

During fracture propagation, the stress intensity factor at the crack tip can be expressed as:

$$K_{\mathrm{I}} = PF\sqrt{\pi(r_{\mathrm{b}} + r)} + \sigma\sqrt{\pi r} \tag{7}$$

where P is the instantaneous detonation-gas pressure acting during fracture propagation; F is the dimensionless geometry correction coefficient for the mode-I stress intensity factor; r is the instantaneous directional-fracture length; and σ is the tangential crack-driving stress induced by shaped-charge action.

As the opening angle of the shaped-charge liner decreases, the energy-concentration effect becomes more pronounced, resulting in stronger stress concentration along the shaped-charge direction. The mode-I stress intensity factor, K_I, at the tip of the initial fracture along the shaped-charge direction is expressed as:

$$K_{\mathrm{I}} = P_3 F\sqrt{\pi(r_{\mathrm{b}} + r_a)} + \sigma\sqrt{\pi r_a} \tag{8}$$

where P_3 is the detonation-gas pressure in the borehole when jet penetration terminates and the detonation products have filled the borehole. For the present blasting condition, P_3 is taken as 234 MPa.

The geometry correction coefficient F accounts for the influence of the blasthole–fracture geometry on the mode-I stress intensity factor. F is a function of the normalized blasthole–fracture dimension and can be expressed as [28]:

$$F = f\left[\frac{r_b + r}{r_b}\right] \tag{9}$$

When $(r_b + r)/r_b > 1.5$, the variation in F becomes small and F approaches unity. For the present condition, r_b = 0.0325 m and r_a = 0.3935 m, giving $(r_b + r_a)/r_b \approx 13.1$, which is substantially greater than 1.5. Therefore, F = 1.0 is adopted in the subsequent fracture-propagation and arrest calculations.

According to fracture mechanics for rock blasting, fracture propagation is initiated when the crack-tip stress intensity factor satisfies $K_I > K_{IC}$, where K_{IC} is the fracture toughness of the rock. For the medium-grained sandstone investigated in this study, K_{IC} = 1.00 MPa·m$^{1/2}$. The fracture-initiation condition can therefore be written as:

$$P_3 > \frac{K_{IC} - \sigma\sqrt{\pi r_a}}{F\sqrt{\pi(r_b + r_a)}} \tag{10}$$

According to the above equations, the condition for sustained fracture propagation in the non-shaped-charge direction can be derived as:

$$P_3 > \frac{K_{IC}}{F\sqrt{\pi(r_b + r_a)}} \tag{11}$$

Shaped-jet penetration generates an additional tangential stress along the shaped-charge direction, thereby reducing the critical pressure required for fracture initiation and subsequent propagation compared with that in the non-shaped-charge direction. As a result, fractures preferentially propagate along the shaped-charge direction. This demonstrates the pronounced directional-fracturing capability of shaped charges and supports their application for active weakening and directional roof cutting in hard roof strata.

3.3. Criteria for Crack Overlap Between Adjacent Blast Holes and Blasthole Spacing Control

During bidirectional shaped-charge blasting, the blast stress wave first induces initial directional fractures along the shaped-charge direction. Detonation gases subsequently penetrate into these fractures and drive their further propagation. Previous studies have shown that blast stress waves mainly govern fracture initiation and early-stage growth, whereas the quasi-static action of detonation gases provides an important driving force for sustained fracture propagation at later stages. Accordingly, the spacing between adjacent boreholes should account for both the initial fracture extent at the early blasting stage and the effective fracture propagation range at the later stage.

To provide sufficient space for the independent development of the initial fractures, the absence of premature complete overlap between adjacent initial directional fractures is taken as the lower-bound constraint on borehole spacing. The center-to-center spacing, S, between adjacent boreholes should therefore satisfy:

$$2(r_b + r_a) \leq S \tag{12}$$

For the present condition, r_b = 0.0325 and r_a = 0.3935 m. Substitution into Equation (12) gives Smin $2(r_b + r_a)$ = 0.852 m; therefore, the theoretical lower bound is taken as approximately 0.85 m. After the initial directional fracture is formed, detonation gases enter the fracture and provide a quasi-static driving pressure for its subsequent extension. As the fracture propagates away from the blasthole, this effective gas pressure progressively decreases. Based on the thick-walled-cylinder approximation adopted in previous studies of gas-driven fracture propagation in shaped-charge blasting [29], the quasi-static detonation-gas pressure at the critical fracture-arrest state can be expressed as

$$P_d = P_3\left(\frac{r_b + r_d}{r_b}\right)^{-2} \tag{13}$$

where P_3 is the detonation-gas pressure at the beginning of the gas-driven fracture-propagation stage, P_d is the effective quasi-static detonation-gas pressure at the critical arrest state, and r_d is the effective directional-fracture length measured outward from the blasthole wall at the critical arrest state.

As fracture propagation continues, the driving effects of the detonation gas and the crack-tip force gradually weaken. When the crack-tip stress intensity factor decreases to the fracture toughness of the rock, the fracture reaches the critical arrest condition. Let r_d denote the effective fracture length along the shaped-charge direction. The fracture-arrest condition can then be expressed as:

$$K_{\mathrm{I}}(r_d) = K_{\mathrm{IC}} = P_d F \sqrt{\pi(r_{\mathrm{b}} + r_d)} + \sigma_d \sqrt{\pi r_d} \tag{14}$$

where σ_d is the residual tangential crack-driving stress at the critical arrest state. During the later gas-driven stage, the residual tangential stress is relatively small compared with the quasi-static detonation-gas pressure and is therefore neglected in estimating the critical arrest length, following the treatment adopted in previous blasting-fracture analyses.

Accordingly, combining Equations (13) and (14) gives a critical effective directional-fracture length of approximately r_d = 0.543 m. To ensure that the effective fractures generated from adjacent boreholes overlap within the inter-borehole region at the later blasting stage, the combined effective fracture ranges on both sides should cover the center-to-center borehole spacing. The theoretical upper limit of the borehole spacing can therefore be obtained as:

$$S \leq 2(r_b + r_d) \tag{15}$$

Using r_b = 0.0325 m and $r_d \approx$ 0.543 m, Equation (15) gives Smax = $2(r_b + r_d) \approx$ 1.15 m. Combining the above constraints gives the theoretical control range for the borehole spacing in bidirectional shaped-charge roof-cutting blasting:

$$2(r_b + r_a) \leq S \leq 2(r_b + r_d) \tag{16}$$

Based on the calculated lower bound of approximately 0.85 m from the initial-fracture constraint and the upper bound of approximately 1.15 m from the critical fracture-arrest and fracture-overlap conditions, a preliminary blasthole-spacing control range of 0.85 m $\leq S \leq$ 1.15 m was obtained for the present medium-grained sandstone and blasting conditions. This theoretically derived interval is used to define the range of the subsequent numerical cases rather than to represent a universal optimum spacing.

4. Numerical Simulation of Blasthole Spacing Optimization for Roof Cutting by Bidirectional Shaped-Charge Blasting

4.1. Numerical Model Development

To evaluate the applicability of the theoretical blasthole-spacing range under multi-blasthole synergistic blasting, a numerical model was established using ANSYS 2022 R2 with the LS-DYNA R13.1.0 solver. The model dimensions were 3000 mm × 2000 mm × 5 mm and comprised rock, explosive, air, and shaped-charge liners. The small model thickness, together with the Z-direction displacement constraints, represents a quasi-two-dimensional solid model of a representative cross-section normal to the blasthole axis under an approximately plane-strain condition. The 5 mm thickness is therefore a numerical idealization for representing the cross-sectional response rather than the actual physical thickness of the fractured roof zone. To account for the in situ stress environment of the ZC1103 working face, an initial in situ stress field was applied to the rock domain prior to detonation. Based on in situ stress measurements at the mine site, a vertical stress of 8.2 MPa and a horizontal stress of 16.2 MPa

were applied to the model. The same initial stress state was adopted for all blasthole-spacing cases to ensure that the differences in the numerical responses were mainly associated with the variation in blasthole spacing rather than with differences in the initial stress condition. The directions and magnitudes of the applied vertical and horizontal stresses are indicated in Figure 6.

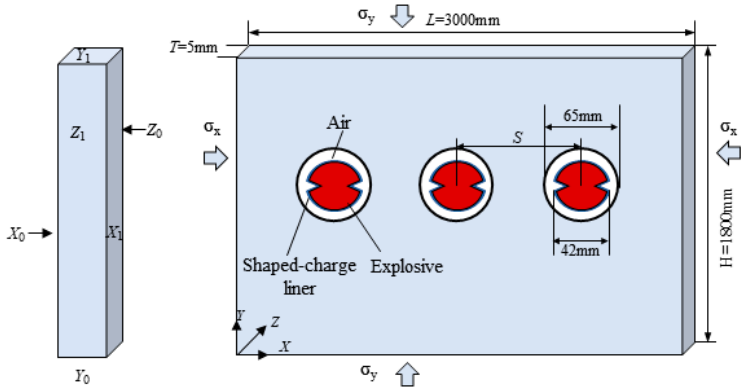


Figure 6. Schematic of the numerical model.

Three boreholes were arranged at equal intervals along the X direction. Each borehole had a diameter of 65 mm, while the shaped-charge liner had an inner diameter of 36 mm and an outer diameter of 42 mm. The shaped openings on both sides were aligned with the line connecting the borehole centers. The explosive and air domains were described using the arbitrary Lagrangian–Eulerian (ALE) formulation to accommodate the large deformation and material flow associated with detonation-product expansion, whereas the rock and shaped-charge liner were modeled using the Lagrangian formulation [21].

To examine the differences in inter-borehole synergistic fracturing when the spacing is below the theoretical lower bound, within the theoretical control range, or above the theoretical upper bound, three spacing cases of 800, 1000, and 1200 mm were selected within and around the theoretical interval. The theoretical analysis was used to constrain the reasonable scale of borehole spacing, while the final spacing was determined by jointly evaluating the inter-borehole stress response and fracture-coalescence characteristics obtained from the numerical simulations.

4.2. Model Boundary Conditions and Key Parameters

The meshes on the Z0 and Z1 planes were constrained using an SPC boundary condition to restrict deformation in the Z direction. Non-reflecting segment boundaries were applied to the X0, X1, Y0, and Y1 faces to minimise the influence of reflected waves from the finite model boundaries on inter-hole stress-wave superposition and fracture propagation [30].

The contact interaction between the shaped-charge liner and the rock was described using an eroding surface-to-surface contact algorithm. Specifically, the *CONTACT_ERODING_SURFACE_TO_SURFACE keyword was employed to define the interaction between the liner and the surrounding rock. To represent localized tensile-dominated failure and the removal of severely damaged rock elements, the minimum-pressure failure criterion in *MAT_ADD_EROSION was adopted. In the present model, MNPRES was set to 7 MPa as the numerical erosion threshold for tensile-dominated local failure of the sandstone. This value serves as a numerical failure and element-removal criterion and is not regarded as a universal material constant.

The explosive was modeled using MAT_HIGH_EXPLOSIVE_BURN, while the pressure–volume–energy relationship of the detonation products was described using the Jones–Wilkins–Lee (JWL) equation of state [31]. The JWL equation of state is expressed as:

$$P_a = A\left(1 - \frac{\omega_1}{R_1 V_1}\right)e^{-R_1 V} + B\left(1 - \frac{\omega_1}{R_2 V_1}\right)e^{-R_2 V} + \frac{\omega_1 E_0}{V_1} \quad (17)$$

where P_a is the detonation pressure of the explosive, GPa; A and B are the JWL pressure constants, GPa; R_1, R_2, and ω_1 are dimensionless parameters; E_0 is the internal energy per unit volume of the detonation products, GJ/m^3; and V_1 is the dimensionless relative volume. The explosive material parameters and the corresponding JWL equation-of-state parameters used in the numerical model are listed in Table 1 [32].

Table 1. Parameters of Explosives and Their Equation of State.

ρ_1	D	P_{CJ}	A	B	R_1	R_2	ω_1	E_0	V_0
1210	5660	9.7	214.4	0.182	4.20	0.90	0.15	4.2	1.0

where ρ_1 is the explosive density, kg/m^3; D is the detonation velocity, m/s; P_{CJ} is the Chapman–Jouguet detonation pressure, GPa; A, B, R_1, R_2, and ω_1 are the JWL equation-of-state parameters; E_0 is the internal energy per unit volume, GJ/m^3; and V_0 is the dimensionless initial relative volume. The rock material parameters adopted in the HJC constitutive model are summarized in Table 2.

Table 2. Rock Material Parameters.

ρ_2	G	Fc	T	A_1	B_1	C	N_1	D_1	D_2
2614	17.4	45	12.5	0.26	1.17	0.007	1.02	0.043	1.00

where ρ_2 is the rock density, kg/m^3; G is the shear modulus, GPa; Fc is the quasi-static uniaxial compressive strength, MPa; T is the maximum tensile strength of the rock, MPa; A_1 is the normalized cohesive strength parameter; B_1 is the normalized pressure-hardening parameter; C is the strain-rate effect parameter; N_1 is the pressure-hardening exponent; and D_1 and D_2 are the dimensionless damage-evolution parameters [33,34].

Air was modeled using *MAT_NULL, and its thermodynamic behavior was described by the *LINEAR_POLYNOMIAL equation of state:

$$P_e = C_0 + C_1\mu + C_2\mu^2 + C_3\mu^3 + (C_4 + C_5\mu + C_6\mu^2)E_1 \quad (18)$$

where P_e is the air pressure, MPa; C_0, C_1, C_2, and C_3 are pressure-dimensional coefficients, MPa; C_4, C_5, and C_6 are dimensionless coefficients; μ is the dimensionless specific-volume strain parameter; and E_1 is the internal energy per unit initial volume, J/m^3. The air material parameters and the corresponding equation-of-state parameters used in the numerical model are listed in Table 3 [35].

Table 3. Parameters of Air and Its Equation of State.

ρ_3	C_0	C_1	C_2	C_3	C_4	C_5	C_6	E_1
1.2	0	0	0	0	0.4	0.4	0	2.5×10^5

where ρ_3 is the air density, kg/m^3.

The shaped-charge liner was made of copper and modeled using the Johnson–Cook constitutive relation to describe its large deformation, high-strain-rate response, and thermal softening under detonation loading [36]. The yield stress in the Johnson–Cook model is expressed as:

$$\sigma_y = \left(A_2 + B_2\varepsilon_p^n\right)\left(1 + C_a \ln \dot{\varepsilon}^*\right)(1 - T^{*m}) \quad (19)$$

where A_2 is the initial yield strength, MPa; B_2 is the strain-hardening coefficient, MPa; ε_p is the equivalent plastic strain; n is the strain-hardening exponent; C_a is the strain-rate sensitivity coefficient; $\dot{\varepsilon}^*$ is the normalized plastic strain rate; m is the thermal-softening exponent; and T^* is the normalized temperature, defined as:

$$T^* = \frac{T_a - T_r}{T_m - T_r} \tag{20}$$

where T_a is the current material temperature, K; T_r is the reference temperature, K; and T_m is the melting temperature of the material, K. The material parameters adopted for the copper shaped-charge liner are listed in Table 4 [37].

Table 4. Parameters of Copper Material.

ρ_4	A_2	B_2	C	n	m	T_m	T_r
8930	90	210	0.025	0.31	1.09	1356	293

where ρ_4 is the density of the copper material, kg/m^3.

5. Numerical Simulation Results and Discussion

5.1. Mesh Sensitivity Analysis

To minimize the influence of mesh discretization on the numerical results and ensure the reliability of the subsequent fracture-propagation analysis, a mesh sensitivity analysis was conducted prior to the simulations involving different blasting configurations and blasthole spacings. A blasthole spacing of 1.0 m was selected as the representative case. Three numerical models with mesh sizes of 0.01, 0.02, and 0.03 m were established while keeping the model geometry, material parameters, boundary conditions, and blasting loads unchanged. Two observation regions with identical dimensions were defined on the left and right sides of the model, as shown in Figure 7. The eroded-area fraction within each observation region was adopted as the quantitative indicator for evaluating the sensitivity of the numerical response to mesh resolution.

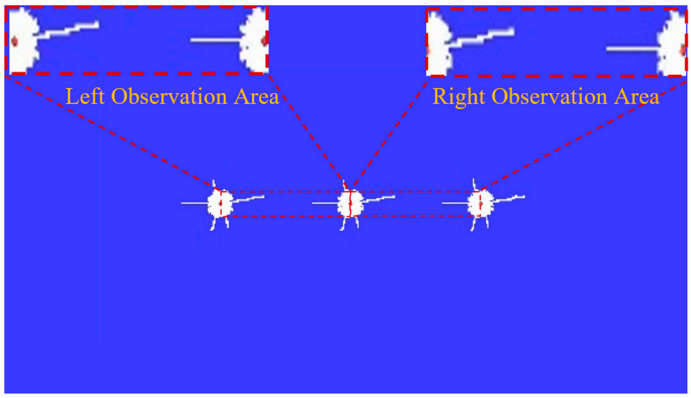


Figure 7. Schematic diagram of observation regions for mesh sensitivity analysis.

As shown in Figure 8, the eroded-area fractions in the left observation region were 7.31%, 7.21%, and 7.29% for mesh sizes of 0.01, 0.02, and 0.03 m, respectively, while the corresponding values in the right observation region were 6.89%, 6.80%, and 6.72%. The differences between the left and right observation regions were 0.42, 0.41, and 0.57 percentage points, respectively. Overall, the eroded-area fractions remained relatively stable within the investigated mesh-size range. In particular, the 0.01 and 0.02 m meshes produced very similar results, and the difference between the two symmetric observation regions was smallest for the 0.02 m mesh. By contrast, although the overall eroded-area fraction obtained with

the 0.03 m mesh remained comparable, the left–right difference increased to 0.57 percentage points, indicating a relatively greater local discrepancy under the coarser discretization.

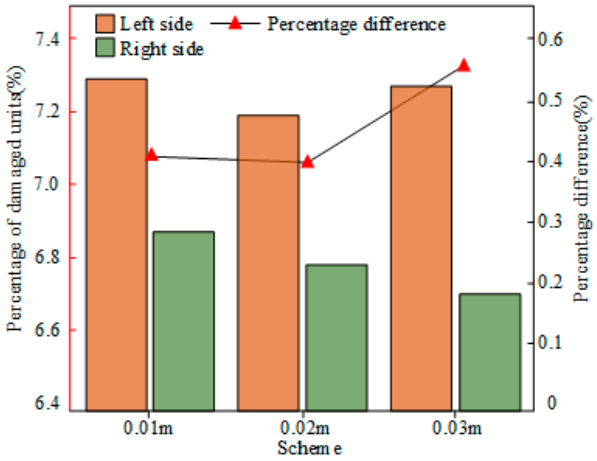


Figure 8. Comparison of eroded-area fractions and left–right differences for different mesh sizes.

Considering both numerical stability and computational efficiency, the 0.02 m mesh was selected for the subsequent simulations. Compared with the finer 0.01 m mesh, the 0.02 m mesh produced only a minor change in the predicted damage response while substantially reducing the computational demand. Meanwhile, it showed better local symmetry than the 0.03 m mesh. Therefore, a mesh size of 0.02 m was considered appropriate for the comparative analysis of fracture propagation and inter-blasthole interaction in this study.

5.2. Fracture Development Under Conventional and Bidirectional Shaped-Charge Blasting

To clarify the directional control exerted by the bidirectional shaped-charge structure on fracture propagation under single-borehole blasting, and to provide a basis for estimating the effective single-borehole influence range for subsequent multi-borehole spacing design, separate numerical models were established for conventional single-borehole blasting and bidirectional shaped-charge blasting. Figures 9 and 10 show the spatial distribution and evolution of eroded/deleted rock elements at 100, 200, and 300 μs for conventional blasting and bidirectional shaped-charge blasting, respectively. The eroded/deleted elements are used to characterize the development of blasting-induced fractures.

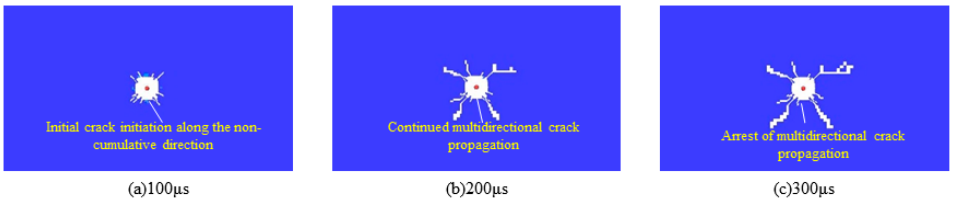


Figure 9. Fracture-development process during conventional single-blasthole blasting.

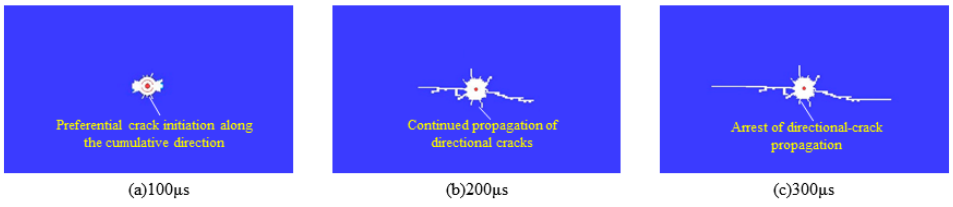


Figure 10. Fracture-development process during bidirectional shaped-charge single-blasthole blasting.

Under conventional blasting, a localized failure zone forms around the borehole at 100 μs, accompanied by several short fractures. By 200 μs, these fractures continue to propagate in multiple directions, with some showing deflection and branching, and their propagation lengths vary with direction. At 300 μs, fracture growth approaches a stable state and the propagation rate decreases markedly, ultimately producing a multidirectional fracture pattern centered on the borehole. These results indicate that conventional blasting produces strongly dispersed fracture propagation with limited directional control.

Under bidirectional shaped-charge blasting, fractures preferentially initiate on both sides of the borehole along the shaped-charge direction at 100 μs. By 200 μs, they continue to extend along this direction and gradually develop into distinct directional main fractures. In contrast, only short fractures form around the borehole in the non-shaped-charge direction, with a limited propagation range. At 300 μs, the main fractures along the shaped-charge direction exhibit greater extension and improved continuity, and fracture growth gradually stabilizes while maintaining the prescribed propagation path. This demonstrates that the bidirectional shaped-charge structure can effectively guide fracture propagation along the designed direction.

To quantitatively evaluate the directional pressure response under different charge configurations, Figure 11 presents the arrangement of pressure monitoring points for the two single-borehole models. In the bidirectional shaped-charge model, points A and B are located along the X-direction shaped-charge axis at distances of 100 and 200 mm from the borehole center, respectively, whereas points C and D are positioned along the Y-direction non-shaped-charge axis at the same distances. In the conventional blasting model, points E and F are arranged along the X direction and points G and H along the Y direction, again at distances of 100 and 200 mm from the borehole center. The complete pressure time histories were extracted at all monitoring points, and the maximum value of each curve was defined as the peak pressure for comparison of pressure attenuation in different directions.

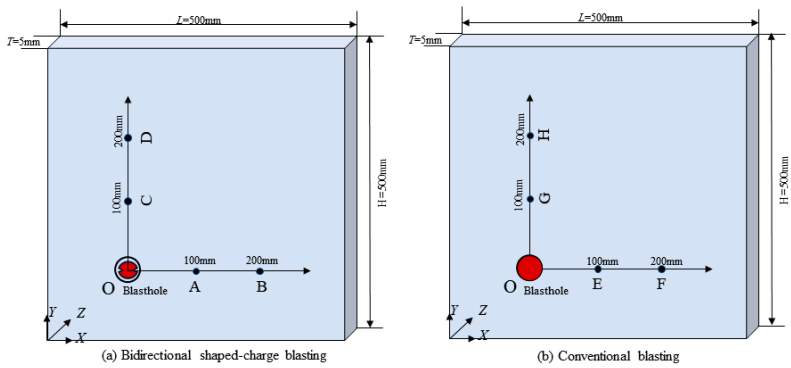


Figure 11. Schematic of pressure-measurement-point arrangements for single blast holes with different charge configurations.

Along the X-direction shaped-charge axis, the peak pressures at 100 and 200 mm from the borehole center were 576.5 and 321.5 MPa, respectively, representing increases of 48.9% and 35.1% relative to conventional blasting at the corresponding locations. The corresponding peak times occurred 60.0 and 28.0 μs earlier. Along the Y-direction non-shaped-charge axis, the peak pressures under bidirectional shaped-charge blasting were 248.5 and 136.9 MPa, respectively, which were 28.0% and 34.9% lower than those under conventional blasting. Their peak times were delayed by 84.0 and 72.0 μs, respectively. Figure 12 compares the pressure time-history curves for single-borehole bidirectional shaped-charge blasting and conventional blasting.

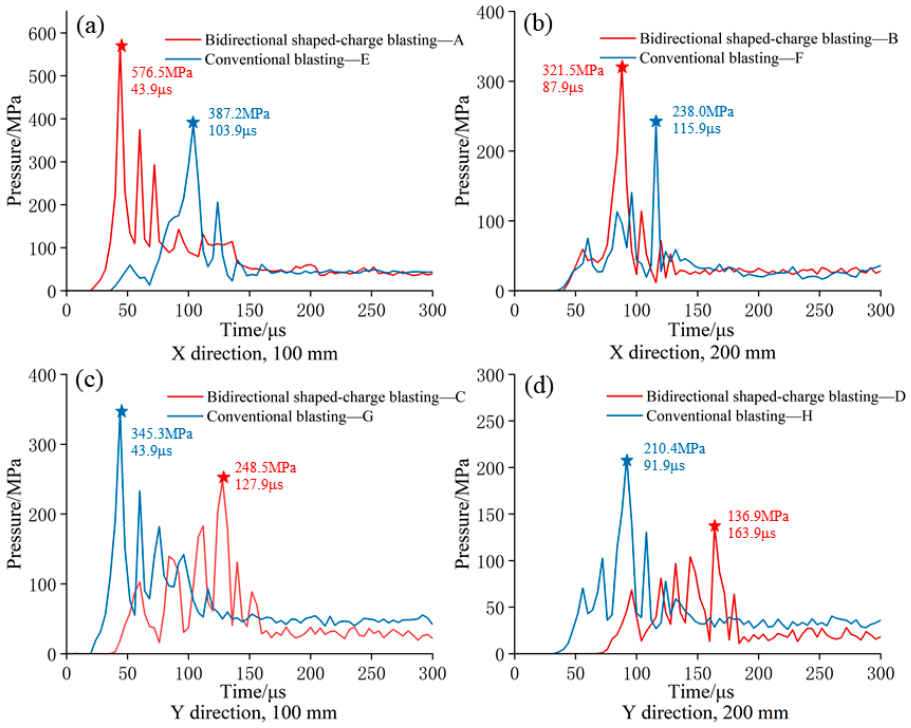


Figure 12. Comparison of pressure–time histories between bidirectional shaped-charge blasting and conventional blasting at different monitoring positions: (**a**) X direction, 100 mm (points A and E); (**b**) X direction, 200 mm (points B and F); (**c**) Y direction, 100 mm (points C and G); (**d**) Y direction, 200 mm (points D and H).

A further comparison of pressure responses in different directions under the same blasting conditions shows that, for conventional blasting, the X-direction peak pressures at 100 and 200 mm were only 12.1% and 13.1% higher than the corresponding Y-direction values, indicating relatively weak directional differences. By contrast, under bidirectional shaped-charge blasting, the X-direction peak pressures were 132.0% and 134.8% higher than those in the Y direction at the same distances, demonstrating pronounced directional pressure redistribution. These results indicate that the bidirectional shaped-charge structure does not enhance pressure uniformly in all directions; instead, it concentrates blast loading along the shaped-charge direction while reducing the pressure response in the non-shaped-charge direction.

5.3. Crack-Development Patterns at Different Blasthole Spacings

To elucidate the effects of borehole spacing on inter-borehole fracture development and coalescence during three-borehole bidirectional shaped-charge blasting, three cases with borehole spacings, S, of 800, 1000, and 1200 mm were considered. Fracture evolution at 100, 200, and 300 μs after detonation was compared, with particular attention to the initiation, propagation, overlap, and coalescence of fractures between adjacent boreholes along the shaped-charge direction, to evaluate the inter-borehole synergistic fracturing effect at different spacings. Figure 13 illustrates the inter-borehole fracture coalescence process for three-borehole bidirectional shaped-charge blasting at different borehole spacings.

To further quantify the influence of blasthole spacing on inter-blasthole fracture development, the inter-blasthole eroded-area fraction was evaluated at 300 μs. The statistical region was restricted to the net rock bridge between the opposing walls of adjacent blastholes. The eroded-area fraction was determined from the initial area of rock elements removed by the erosion criterion relative to the total initial rock area within the same rock-bridge region, excluding the original blasthole cavities. The same region-definition

rule, vertical statistical height, mesh resolution, erosion criterion, and analysis time were adopted for all three spacing cases.

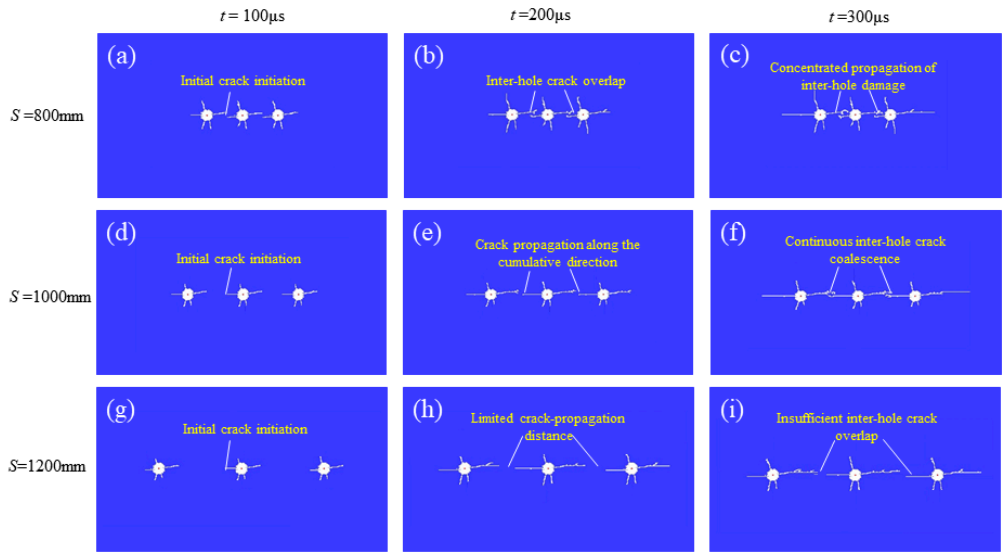


Figure 13. Inter-hole crack evolution at different blasthole spacings (S = 800, 1000, and 1200 mm) and times (t = 100, 200, and 300 μs): (**a**) initial cracking; (**b**) crack overlap; (**c**) concentrated damage propagation; (**d**) initial cracking; (**e**) directional crack propagation; (**f**) continuous crack coalescence; (**g**) initial cracking; (**h**) limited crack propagation; (**i**) insufficient crack overlap.

The inter-blasthole eroded-area fractions for the 0.8, 1.0, and 1.2 m spacing cases were 7.31%, 6.15%, and 3.12%, respectively. At 0.8 m, strong interaction between adjacent blastholes resulted in extensive overlap of the inter-blasthole damaged regions. At 1.0 m, continuous inter-blasthole fracture coalescence was also achieved, while the eroded-area fraction decreased markedly. In contrast, although the 1.2 m case exhibited the lowest eroded-area fraction, the fractures propagating from adjacent blastholes showed insufficient overlap at 300 μs, indicating inadequate inter-blasthole fracture development.

For the 0.8 and 1.0 m cases, which both achieved continuous inter-blasthole fracture development, Figure 13 further shows that the 0.8 m case exhibited more pronounced secondary and off-direction damage around the principal fracture path. In comparison, the damage pattern at 1.0 m was relatively more concentrated along the intended direction. Therefore, among the three tested configurations, the 1.0 m spacing provided a more favorable balance between continuous directional fracture development and control of surrounding local damage. It should be noted that the present comparison was limited to the investigated spacings of 0.8, 1.0, and 1.2 m and therefore does not establish a universal optimum.

5.4. Pressure-Field Evolution at Different Blasthole Spacings

To further elucidate the effects of borehole spacing on pressure-field evolution during bidirectional shaped-charge blasting, pressure contour maps at 50, 100, 200, and 300 μs after detonation were compared. The analysis focused on the propagation, superposition, and attenuation of blast-induced pressure waves around the boreholes and in the inter-borehole region, thereby characterizing inter-borehole pressure-field interactions at different borehole spacings. Figure 14 shows the pressure evolution during bidirectional shaped-charge blasting at different borehole spacings.

Under all spacing conditions, the pressure field underwent a sequence of pressure concentration around the boreholes, outward pressure-wave propagation, inter-borehole pressure superposition, and pressure-field attenuation and diffusion. At 50 μs after detonation,

local high-pressure zones had formed around each borehole, whereas the inter-borehole pressure fields had not yet interacted. By 100 μs, the blast-induced pressure waves had continued to propagate outward, and the inter-borehole regions had begun to experience the combined action of pressure waves from adjacent boreholes.

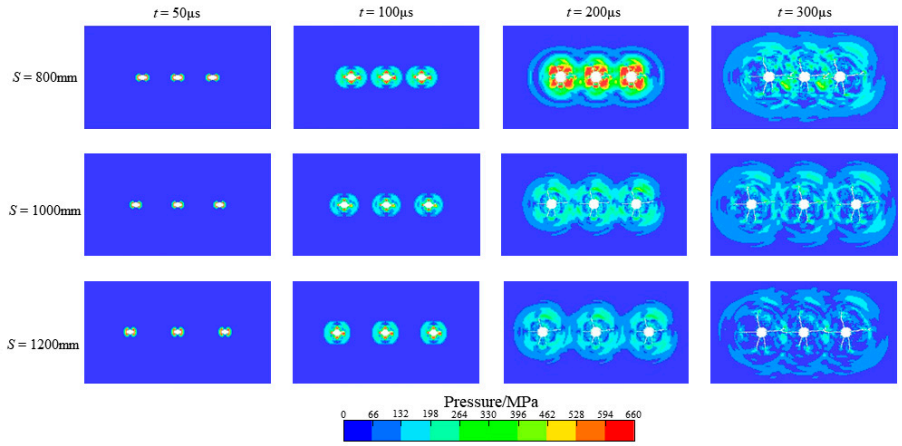


Figure 14. Evolution of inter-hole pressure-wave superposition in three-blasthole bidirectional Shaped-Charge Blasting at different blasthole spacings.

At 200 μs, differences in inter-borehole pressure superposition became evident among the spacing conditions. At a borehole spacing of 800 mm, the pressure fields of adjacent boreholes overlapped, forming a continuous high-pressure superposition zone in the inter-borehole region. At 1000 mm, pressure waves from adjacent boreholes also overlapped in the inter-borehole region, but both the overlap range and pressure concentration were weaker than those at 800 mm. When the spacing increased to 1200 mm, the high-pressure zones around individual boreholes remained relatively isolated, and inter-borehole pressure superposition was weak.

By 300 μs, the pressure waves in all cases had continued to propagate outward and gradually attenuated, although differences in the inter-borehole pressure fields remained. At 800 mm, a broad continuous pressure-superposition zone had formed between adjacent boreholes. At 1000 mm, the inter-borehole pressure fields achieved effective overlap. In contrast, pressure superposition remained insufficient in the inter-borehole region at 1200 mm. These results indicate that increasing borehole spacing enhanced the attenuation of blast-induced pressure waves and weakened inter-borehole pressure superposition, which hindered the formation of a continuous synergistic interaction zone between adjacent boreholes.

6. Field Validation of Fracture Development and Pressure-Relief Effectiveness

To evaluate the field applicability of the selected 1.0 m blasthole spacing, field observations were conducted from two complementary perspectives. Borehole imaging was used to compare local inter-blasthole fracture development under different spacings, while roadway surrounding-rock deformation monitoring was used to evaluate the engineering pressure-relief performance of the roof-cutting treatment. Together, these observations provide field-scale support for the local fracture-development characteristics and deformation-control performance under the investigated conditions.

6.1. Borehole-Imaging Observations of Local Fracture Development

To compare local fracture development between adjacent blastholes under different spacing conditions, a borehole imaging test was conducted in a test section of the return

airway at the ZC1103 working face. Four blastholes were sequentially arranged along the working-face advance direction, with adjacent blasthole spacings of 0.8, 1.0, and 1.2 m. An observation borehole was positioned at the midpoint between each pair of adjacent blastholes, corresponding to distances of 0.4, 0.5, and 0.6 m from the neighboring blastholes, respectively. The Shaped-Charge directions were aligned with the lines connecting adjacent blastholes, allowing the directional fractures generated from neighboring blastholes to propagate toward each other through the inter-hole rock mass. After blasting, the fracture characteristics observed on the borehole walls were used to qualitatively compare local fracture development between adjacent blastholes at different spacings. The three observation locations were situated within the same roof stratum of the ZC1103 return airway and had generally similar lithological and structural conditions, providing a basis for comparison of local fracture development. The borehole layout is shown in Figure 15. Borehole images were obtained using a GD3Q-GA6 borehole imaging system. The observation boreholes were drilled upward into the roof, and the images used for comparison were collected at a consistent depth of 16 m measured along the borehole axis from the collar. Fractures were identified from clearly visible discontinuities and openings on the borehole wall.

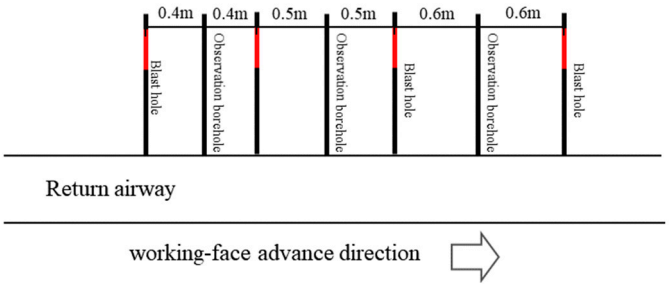
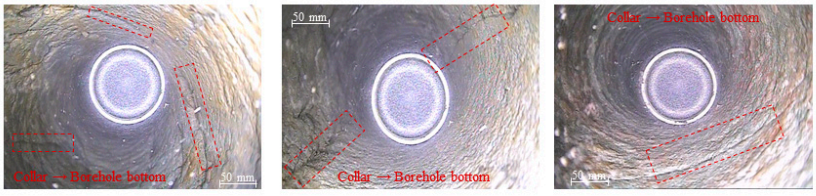


Figure 15. Schematic of borehole-imaging measurement-point arrangements for bidirectional Shaped-Charge Blasting.

As shown in Figure 16, the local fracture development observed in the inter-blasthole observation boreholes varies with blasthole spacing. At a spacing of 0.8 m, several fracture traces are visible on the borehole wall, indicating relatively pronounced local fracture development. When the spacing increases to 1.0 m, distinct fracture traces are observed, while the borehole wall outside the main fracture zones remains relatively intact. At a spacing of 1.2 m, fracture development is less pronounced in the presented image. These observations provide local field evidence of fracture development between adjacent blastholes and qualitatively supplement the numerical results. However, because only one observation borehole was examined for each spacing, the borehole images do not independently demonstrate the formation of a continuous fracture plane across the entire inter-blasthole rock bridge.



(a) Blasthole spacing of 0.8 m (b) Blasthole spacing of 1.0 m (c) Blasthole spacing of 1.2 m

Figure 16. Borehole images showing local fracture development at a consistent observation depth of 16 m under different blasthole spacings.

6.2. Monitoring of Roadway Surrounding-Rock Deformation

Roadway deformation monitoring stations were installed at 50 m intervals along the tailgate of the ZC1103 working face. For the comparative analysis, representative monitoring stations were selected based on two criteria: a clear difference in roof-cutting treatment and the comparability of the principal site conditions. Accordingly, the monitoring stations at chainages 1150 and 1300 m were selected to represent the non-roof-cutting and roof-cutting zones, respectively, with a separation distance of 150 m. Both monitoring sections were located along the same tailgate and had comparable geological conditions and burial depths, while the roadway cross-section and support conditions were essentially consistent. These conditions provided a reasonable basis for comparing the surrounding-rock deformation between the roof-cutting and non-roof-cutting zones. Roadway convergence was monitored using the cross-measurement method. Owing to loose-coal accumulation on the roadway floor and disturbance caused by floor denting, only roof subsidence was analyzed for the vertical deformation, rather than roof-to-floor convergence.

To evaluate the field performance of the roof-cutting and pressure-relief treatment using the selected 1.0 m blasthole spacing, the cumulative surrounding-rock deformation in the pressure-relief and non-pressure-relief zones was comparatively analyzed.

Figure 17 compares the cumulative deformation of the surrounding rock in the roof-cutting and pressure-relief zone with that in the non-pressure-relief zone after bidirectional shaped-charge blasting. Over the same monitoring period, cumulative deformation of the roof, solid-coal rib, and gob-side rib increased with time in both zones; however, the deformation curves for the roof-cutting and pressure-relief zone remained consistently below those for the non-pressure-relief zone. In the non-pressure-relief zone, the cumulative deformation of the solid-coal rib, gob-side rib, and roof reached 360, 610, and 162 mm, respectively, compared with 210, 294, and 99 mm in the roof-cutting and pressure-relief zone. These values correspond to reductions of 41.7%, 51.8%, and 38.9%, respectively. The gob-side rib exhibited both the greatest deformation and the largest reduction.

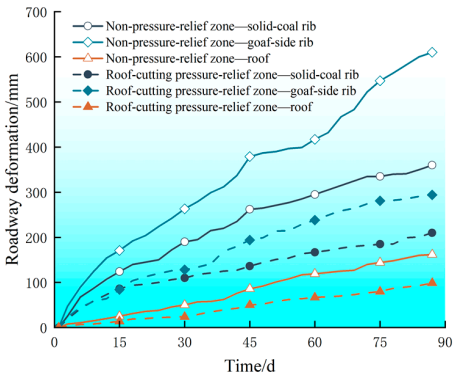


Figure 17. Comparison of cumulative surrounding-rock deformation between the roof-cutting pressure-relief zone and the non-pressure-relief zone following bidirectional Shaped-Charge Blasting.

Overall, lower cumulative deformation was observed for all three surrounding-rock components in the roof-cutting and pressure-relief zone than in the non-pressure-relief zone, with the most pronounced difference occurring at the gob-side rib. These deformation differences reflect the overall effect of the roof-cutting and pressure-relief treatment under the investigated field conditions and should not be attributed exclusively to the selected 1.0 m blasthole spacing.

7. Conclusions

(1) For borehole-spacing design in bidirectional shaped-charge blasting of thick and hard roofs, a theoretical spacing range of 0.85–1.15 m was derived by considering the effective propagation range of fractures generated by a single borehole, attenuation of blast-induced pressure waves, interactions between adjacent fracture tips, and the overlap of inter-borehole damage zones. The central borehole was jointly affected by the adjacent boreholes on both sides, allowing the model to capture two-sided synergistic fracturing within a continuous borehole array and providing a theoretical basis for selecting numerical simulation conditions.

(2) The bidirectional shaped-charge structure altered the spatial distribution of blasting pressure around the borehole. At distances of 100 and 200 mm from the blasthole center, peak pressures in the shaped-charge direction were 48.9% and 35.1% higher, respectively, than those under conventional blasting, whereas peak pressures in the non-shaped-charge direction were 28.0% and 34.9% lower. Primary fractures propagated preferentially along the non-shaped-charge direction, while secondary fractures in the conventional direction exhibited more limited propagation, indicating a pronounced directional-fracturing effect.

(3) At 300 μs, the 0.8 and 1.0 m spacing cases both achieved continuous inter-blasthole fracture coalescence. At a spacing of 1.2 m, directional fractures developed from individual blastholes, but their propagation ranges did not sufficiently overlap across the inter-blasthole rock bridge, and continuous inter-blasthole fracture coalescence was therefore not achieved. Although the 0.8 m case also satisfied the connectivity requirement, it exhibited a higher inter-blasthole eroded-area fraction and more pronounced secondary damage around the principal fracture path. The 1.0 m spacing maintained continuous directional fracture development with a lower overall level of rock erosion and a relatively more concentrated damage pattern. Therefore, under the investigated conditions, 1.0 m was the best-performing configuration among the three tested spacing cases rather than a universal optimum.

(4) Field trials of bidirectional shaped-charge blasting for roof cutting and pressure relief were conducted at a blasthole spacing of 1.0 m. Distinct fracture traces were observed on the wall of the observation borehole located 0.5 m from the adjacent blasthole, while the surrounding borehole wall remained largely intact, providing local field evidence of directional fracture development. Compared with the non-pressure-relief zone, the cumulative deformations of the solid-coal rib, gob-side rib, and roof in the roof-cutting pressure-relief zone decreased by 41.7%, 51.8%, and 38.9%, respectively. These deformation reductions reflect the overall response to the roof-cutting and pressure-relief treatment under the investigated field conditions and should not be attributed exclusively to the selected 1.0 m blasthole spacing.

Author Contributions: Conceptualization, P.S. and Y.M.; methodology, X.W. (Xiaomin Wang) and K.C.; software, Y.M. and X.W. (Xiaochen Wu); validation, P.S. and W.Y.; formal analysis, Y.M. and X.W. (Xiaomin Wang); investigation, H.X. and W.Y. Resources, W.W. data curation, X.W. (Xiaomin Wang) and Y.M. writing—original draft preparation, H.X., Y.M. and W.W. writing—review and editing, P.S. and H.X. supervision, P.S. Project administration, H.X. Funding acquisition, P.S. and H.X. All authors have read and agreed to the published version of the manuscript.

Funding: This work was financially supported by the Deep Earth Probe and Mineral Resources Exploration-National Science and Technology Major Project (No. 2024ZD1004503), the National Natural Science Foundation of China (Nos. 52574162 and 52404142), the China Postdoctoral Science Foundation (No. 2025T180506), and the Yulin Science and Technology Plan Project (No. 2024-CXY-163 and No. 2024-CXY-164). Shaanxi Provincial Postdoctoral Research Project (Grant No.

2024BSHYDZZ017) and the Natural Science Basic Research Program of Shaanxi Province (Grant No. 2026JC-YBMS-0602).

Data Availability Statement: Data will be made available on request.

Conflicts of Interest: Author Xiaochen Wu and Kun Chen and Wenlin Wang were employed by the company Shaanxi Huabin Yadian Coal Industry Co., Ltd. The remaining authors declare that the research was conducted in the absence of any commercial or financial relationships that could be construed as a potential conflict of interest.

References

1. Xie, H. Research review of the state key research development program of China: Deep rock mechanics and mining theory. *J. China Coal Soc.* **2019**, *44*, 1283–1305.
2. Xu, H.; Li, K.; Lai, X.; Shan, P.; Zhang, B.; Dai, L.; Yang, S.; Guo, Q.; Xi, X.; Yan, Z. Intelligent prediction method of rockburst driven by microseismic temporal features in deep near-vertical coal seams. *Int. J. Miner. Metall. Mater.* **2026**, *33*, 2403–2418. [CrossRef]
3. Li, J.; Wang, C.; Liu, D.; He, M.; Zhu, C.; Guo, Y.; Sun, L. Experimental investigation on the role of stress difference in rapid unloading response and delayed strainburst failure under true triaxial conditions. *Rock Mech. Rock Eng.* **2026**. [CrossRef]
4. Xie, S.; Wu, Y.; Guo, F.; Zou, H.; Chen, D.; Zhang, X.; Ma, X.; Liu, R.; Wu, C. Application of pre-splitting and roof-cutting control technology in coal mining: A review of technology. *Energies* **2022**, *15*, 6489. [CrossRef]
5. Xu, H.; Li, K.; Zhang, B.; Zhan, R.; Yang, S.; Xi, X.; Dai, L. Thermo-mechanical damage characteristics and fracture behavior of backfill bodies in thermal energy storage cavities: An experimental and numerical study. *Tunn. Undergr. Space Technol.* **2026**, *175*, 107715. [CrossRef]
6. Xu, G.; Lai, X.; Shan, P.; Xu, H. Study on the damage mechanism and instability precursor of high temperature water-cooled granite based on acoustic emission response characteristics. *Eng. Fract. Mech.* **2026**, 112728. [CrossRef]
7. Wang, J.; Liu, P.; Liu, S.; Ma, L.; Liu, Y.; Chen, X. Study on collaborative pressure relief control technology for surrounding rock stability of dynamic pressure roadway in coal mine. *J. Min. Sci. Technol.* **2021**, *6*, 323–332.
8. Zhao, S. Mechanism and application of force–structure cooperative prevention and control of rockburst with deep-hole roof pre-blasting. *J. China Coal Soc.* **2021**, *46*, 3419–3432.
9. Dai, L.; Zhao, X.; Pan, Y.; Wang, A.; Lu, C.; Xu, H. A new evaluation method of active energy-releasing capacity of boreholes for roadway rockburst mitigation. *Rock Mech. Rock Eng.* **2026**. [CrossRef]
10. Li, Y.; Ni, T.; Zuo, J.; Liu, D.; Song, Y. Analysis of crack initiation mechanism and influencing factors of hard roofs due to directional hydraulic fracturing. *Chin. J. Rock Mech. Eng.* **2022**, *41*, 2015–2029.
11. Zhuang, J.; Mu, Z.; Cai, W.; He, H.; Hosking, L.J.; Xi, G.; Jiao, B. Multistage hydraulic fracturing of a horizontal well for hard roof related coal burst control: Insights from numerical modelling to field application. *Int. J. Min. Sci. Technol.* **2024**, *34*, 1095–1114. [CrossRef]
12. Liu, S.; Li, X.; Fu, M.; He, Y.; Pan, K.; Hou, B.; He, D. Mechanism of Roof-Cutting by Densely Drilled Holes in Gob-Side Entry Retaining and Its Main Influencing Factors. *Energy Sci. Eng.* **2025**, *13*, 4794–4809. [CrossRef]
13. Ma, J.; Wang, H.; Li, X.; Dong, G.; Yuan, Y. Design and application study of the key technical parameters of dense drilling for pressure relief in coal mine roofs: A case study. *Sci. Rep.* **2026**, *16*, 18141. [CrossRef] [PubMed]
14. Zhu, F.; Liu, Z.; Zuo, Y.; Yang, N.; Huang, A.-C. Damage and failure characteristics of coal and surrounding rock under shaped blasting. *Process Saf. Environ. Prot.* **2023**, *176*, 56–64. [CrossRef]
15. Liu, X.; He, X.; Liang, Y.; Hua, X.; Li, C. Study on cracking mechanism and key parameters of roof in gob-side entry retaining by pre-split blasting roof in deep mine. *Energy Explor. Exploit.* **2025**, *43*, 47–64. [CrossRef]
16. Sun, B.-J.; Hua, X.-Z.; Zhang, Y.; Yin, J.; He, K.; Zhao, C.; Li, Y. Analysis of Roof Deformation Mechanism and Control Measures with Roof Cutting and Pressure Releasing in Gob-Side Entry Retaining. *Shock Vib.* **2021**, *2021*, 6677407. [CrossRef]
17. Yu, B.; Tai, Y.; Li, Y.; Kuang, T.; Zhang, W.; Meng, X. An innovative technology of directional roof slitting by composite blasting and an engineering application. *J. China Coal Soc.* **2023**, *48*, 126–138.
18. Ma, B.; Tai, Y.; Li, Y.; Xia, H.; Meng, X. Investigation of the process of perforating hard roof in an innovative technology of directional roof-cutting by composite blasting. *Energy Sci. Eng.* **2023**, *11*, 2585–2600. [CrossRef]
19. Liu, K.; Zhang, Y.P.; Peng, Y.; Wu, L. Experimental research and application of drilling and blasting with directional damage-reduction shaped charge. *Sci. Rep.* **2024**, *14*, 9549. [CrossRef] [PubMed]
20. Ding, C.; Yang, R.; Feng, C. Stress wave superposition effect and crack initiation mechanism between two adjacent boreholes. *Int. J. Rock Mech. Min. Sci.* **2021**, *138*, 104622. [CrossRef]

21. Meng, N.; Bai, J.; Yoo, C.-S.; Chen, Y. Effects of in-situ stress and delay time on rock damage under shaped charge jet blasting. *J. Cent. South Univ.* **2023**, *30*, 1359–1372. [CrossRef]
22. Meng, N.; Chen, Y.; Bai, J.; Wang, X.; Wu, W.; Wu, B. Numerical simulation of directional fracturing by shaped charge blasting. *Energy Sci. Eng.* **2020**, *8*, 1824–1839. [CrossRef]
23. Wu, B.; Xu, S.; Meng, G.; Cai, J.; Wei, H.; Li, H.; Zhang, J. Study on Dynamic Evolution Law of Blasting Cracks in Elliptical Bipolar Linear Shaped Charge Blasting. *Shock Vib.* **2021**, *2021*, 5272878. [CrossRef]
24. Li, Y.; Chang, G.; Hu, D.; Song, W. Application of pre-splitting blasting roof-cutting pressure relief technology for roadway protection under hard roof. *Sci. Rep.* **2025**, *15*, 25458. [CrossRef] [PubMed]
25. Yue, G.; Li, M.; Wang, L.; Liang, W. Optimal layout of blasting holes in structural anisotropic coal seam. *PLoS ONE* **2019**, *14*, e0218105. [CrossRef] [PubMed]
26. Rong, H.; Li, N.; Cao, C.; Wang, Y.; Li, J.; Li, M. Numerical simulation of blasting behavior of rock mass with cavity under high in-situ stress. *Sci. Rep.* **2024**, *14*, 16046. [CrossRef] [PubMed]
27. Wang, K.; Zhang, C.; Hao, B.; Zhang, S. Study on initiation and propagation mechanism of internal cracks caused by dynamic and static action of shaped charge blasting under in-situ stress. *Coal Sci. Technol.* **2023**, *51*, 50–64.
28. Gao, H.; Gao, Y.; Wang, J.; Fu, Q.; Qiao, B.; Wei, X.; Zhang, X. Study on bidirectional blasting technology for composite sandstone roof in gob-side entry-retaining mining method. *Appl. Sci.* **2021**, *11*, 7524. [CrossRef]
29. Shi, Q.; Zheng, H.; Wang, Y.; Yun, M.; Wu, S.; Li, T.; Zhang, H. Study on parameters of blast hole spacing for gob side entry retaining by bidirectional shaped charge blasting. *Saf. Coal Mines* **2022**, *53*, 219–225.
30. Wu, B.; Xu, S.; Meng, G.; Cui, Y.; Cai, J.; Zhang, Y. Study on the Dynamic Evolution of Through-Crack in the Double Hole of Elliptical Bipolar Linear-Shaped Charge Blasting. *Shock Vib.* **2021**, *2021*, 3792765. [CrossRef]
31. Lee, E.L.; Hornig, H.C.; Kury, J.W. *Adiabatic Expansion of High Explosive Detonation Products*; Lawrence Radiation Laboratory, University of California: Livermore, CA, USA, 1968.
32. Liu, K.; Qiu, J. Investigation of Burn Cut Parameters and Model for One-Step Raise Excavation Based on Damage Evolution Mechanisms. *Geofluids* **2020**, *2020*, 8879477. [CrossRef]
33. Wei, S.; Li, J.; Wang, M.; Yu, C. Parameter determination and numerical simulation of the sandstone HJC constitutive model. *ACS Omega* **2025**, *10*, 18744–18752. [CrossRef] [PubMed]
34. Tianlong, L.; Shuaifeng, W.; Dianshu, L.; Shufeng, L.; Chen, L.; Jianhui, M. Determination of Holmquist-Johnson-Cook model parameters for sandstone. *J. China Coal Soc.* **2018**, *43*, 2211–2216.
35. Xie, L.; Dong, Z.; Qi, Y.; Qiu, R.; He, Q. Vibration failure of young low-temperature concrete shaft linings caused by blasting excavation. *Adv. Civ. Eng.* **2019**, *2019*, 5343618. [CrossRef]
36. Johnson, G.R.; Cook, W.H. A Constitutive Model and Data for Metals Subjected to Large Strains, High Strain Rates and High Temperatures. In Proceedings of the 7th International Symposium on Ballistics, The Hague, The Netherlands, 19–21 April 1983.
37. Du, Y.; He, G.; Li, W.; Wang, K. Experimental and Numerical Study on the Penetration Performance of a Shaped Charge. *Materials* **2022**, *15*, 3899. [CrossRef] [PubMed]

Disclaimer/Publisher's Note: The statements, opinions and data contained in all publications are solely those of the individual author(s) and contributor(s) and not of MDPI and/or the editor(s). MDPI and/or the editor(s) disclaim responsibility for any injury to people or property resulting from any ideas, methods, instructions or products referred to in the content.